

An immersed boundary method for fluid-structure interaction based on overlapping domain decomposition

Maria Giuseppina Chiara Nestola^{a,1,*}, Barna Becsek^{b,1}, Hadi Zolfaghari^b,
Patrick Zulian^a, Dario De Marinis^b, Rolf Krause^a, Dominik Obrist^b

^a*Institute of Computational Science, Center for Computational Medicine in Cardiology (CCMC), Università della Svizzera Italiana, Via Giuseppe Buffi 13, 9600 Lugano, Switzerland*

^b*ARTORG Center for Biomedical Engineering Research, University of Bern, Murtenstrasse 50, 3008 Bern, Switzerland*

Abstract

We present a novel framework inspired by the Immersed Boundary Method for predicting the fluid-structure interaction of complex structures immersed in flows with moderate to high Reynolds numbers.

The main novelties of the proposed fluid-structure interaction framework are 1) the use of elastodynamics equations for the structure, 2) the use of a high-order Navier–Stokes solver for the flow, and 3) the variational transfer (L^2 -projection) for coupling the solid and fluid subproblems.

The dynamic behavior of a deformable structure is simulated in a finite element framework by adopting a fully implicit scheme for its temporal integration. It allows for mechanical constitutive laws including nonhomogeneous and fiber-reinforced materials.

The Navier–Stokes equations for the incompressible flow are discretized with high-order finite differences which allow for the direct numerical simulation of laminar, transitional and turbulent flows.

The structure and the flow solvers are coupled by using an L^2 -projection method for the transfer of velocities and forces between the fluid grid and the solid mesh. This strategy allows for the numerical solution of coupled large scale

*Corresponding author. *E-mail address:* nestom@usi.ch

¹Both authors contributed equally to the manuscript

problems based on nonconforming structured and unstructured grids.

The framework is validated with the Turek–Hron benchmark and a newly proposed benchmark modelling the flow-induced oscillation of an inert plate. A three-dimensional simulation of an elastic beam in transitional flow is provided to show the solver’s capability of coping with anisotropic elastic structures immersed in complex fluid flow.

Keywords: Fluid-Structure Interaction, Immersed-Boundary Method, Computational Fluid Dynamics, Computational Solid Dynamics, L^2 -Projection

1. Introduction

Over the past decades, Fluid-Structure Interaction (FSI) [1, 2, 3] analysis of the cardiovascular system and, in particular, of heart valves has become an increasingly active area of research [4, 5, 6, 7, 8, 9]. The main difficulties related to numerical simulation of FSI problems are: (a) the existence of a two-field problem where the two phases (i.e. fluid and structure) are separated by a common boundary whose position is an unknown of the problem (geometrical nonlinearity); (b) the treatment of the interface conditions ensuring the continuity of the velocity and the stress across the interface [10]; (c) the interaction with thin and/or bulky solid structures which may exhibit large deformations, and (d) the simulation of moderate- to high-Reynolds-number flows involving transition from laminar to turbulent flow. Moreover, high-fidelity simulations of complex and large-scale problems, such as the interaction between blood flow and heart valves, demand for the development of high-performance numerical libraries. Such libraries are optimized for modern supercomputers by ensuring a high level of parallelism, scalability, flexibility, and efficiency.

In literature, several approaches have been developed for FSI simulations, which can be classified in boundary-fitted [11] and embedded-boundary methods [12, 13].

In boundary-fitted methods, the fluid subproblem is solved in a moving spatial domain where the Navier–Stokes equations are formulated in an Arbitrary

Lagrangian Eulerian framework [11, 14] while the solid structure is usually analyzed in a Lagrangian fashion. Although this approach is known to produce accurate results at the interface between solid and fluid, the fluid grid may become severely distorted for scenarios that involve large displacements and/or rotations, such that the numerical stability of the coupled problem and the accuracy of the solution can be affected. In particular, in heart valve simulations, it can become computationally very expensive to preserve good mesh quality because the movement of the valve leaflets and their contact during valve closure change the topology of the fluid domain.

In order to circumvent those difficulties, embedded-boundary approaches such as the Immersed Boundary Method (IBM) have been introduced for simulating the complex dynamics of the heart. The main characteristic of this approach is the representation of the immersed structure by a force density term in the Navier–Stokes equations.

In the original IBM Peskin [2] adopted a finite difference scheme for the spatial discretization of the fluid subproblem and a Lagrangian model with one-dimensional fiber-like elements for the structure. The solid and the fluid subproblems were coupled by interaction equations involving a smoothed approximation of the Dirac-delta function to interpolate data between Eulerian flow and Lagrangian structure variables.

Since the original development of this method by Peskin, a large number of modified approaches were proposed to simulate flow over geometries on nonconforming grids.

Devendran and Peskin [15] developed an energy functional based version of the conventional IBM that allows for a nodal approximation of the elastic forces generated by an immersed hyperelastic material via a finite element type approximation. Griffith et al. [16] introduced a version of the IBM describing the solid body motion via standard Lagrangian finite element methods. Rather than spreading forces from the nodes of the Lagrangian mesh and interpolating velocities to those mesh nodes, forces are spread from (and velocities are interpolated to) dynamically selected quadrature points defined within the Lagrangian

structural elements.

Other approaches include the potential embedded method whose main idea is modelling the structure via a potential energy and the sharp-interface methodology [17, 18] where the use of a multidimensional ghost-cell technique allows to satisfy the boundary conditions precisely, avoiding spurious spreading of boundary forcing into the fluid.

In the Immersed Finite Element Method (IFEM) the discretization of both the fluid and the solid subproblems are formulated in a finite element fashion [19, 20, 13]. Glowinski et al. [20] adopted the reproducing kernel particle method (RKPM) to approximate the Dirac-delta distribution for interpolating the fluid velocities from Eulerian (fluid) to Lagrangian (structure) coordinates and spreading the interaction forces from the solid mesh to the fluid grid. Boffi et al. [19] introduced natural interpolation operators between fluid and structure discrete spaces. Baaijens et al. [21] proposed the mortar element method for imposing a velocity continuity on the FSI interface with the use of Lagrangian multipliers. This approach was generalized by Hesch et al. [22] for enforcing the velocity constraint over the entire overlapping region between fluid and solid domain. A very similar approach based on Nitsche’s Method [23] was proposed by Kamensky et al. [4] with the difference of restricting the coupling to the structure boundary.

In this work, we describe a novel FSI formulation based on the IBM. We employ a finite difference method for discretizing the incompressible flow and couple it with a finite element method for the full elastodynamics equations of the structural problem by using an L^2 -projection approach for handling the interface conditions [24], namely the velocity continuity and force exchange. The framework is capable of coping with general constitutive characteristics (including anisotropic materials) and complex flow configurations.

The algorithmic framework allows for the transfer of discrete fields between unstructured and structured meshes, which can be arbitrarily distributed among processors. This ensures convergence, efficiency, flexibility, load balancing, and accuracy without requiring a priori information on the relation between the

different meshes. Therefore, the approach introduced in this work is well suited for coupling already existing flow and structure solvers (legacy solvers).

The main novelties of the proposed method may be summarized as follows:

1. The transfer of data between the Eulerian finite difference grid of the fluid and the Lagrangian finite element mesh of the structure is achieved by a fully variational approach, which does not require the use of pointwise interpolation schemes as in the classical IBM.
2. The solid motion is modelled by solving the elastodynamics equation via a fully implicit time-integration scheme, whereas other implementations of IBM derive the motion of the solid structure from the fluid velocity field [16] or describe it through simplified kinematic equations [18].
3. The use of a high-order Navier–Stokes solver allows for direct numerical simulations (DNS) of laminar, transitional and turbulent flows.

For constructing the transfer operator a partition of unity is assigned to each point of the fluid grid [25], i.e. basis functions are attached to the fluid grid. We further introduce a new analytical benchmark problem for the verification of the correct implementation of inertial forces.

The article is divided into five sections. Following this introduction, the fundamental equations governing the FSI problem are presented (Section 2). The second part of Section 2 is dedicated to the description of the coupling strategy and provides details about the variational transfer. Section 3 describes the entire framework and illustrates the FSI algorithm with a flow chart. Numerical results for various benchmark problems are presented and analyzed in Section 4. Finally, some concluding remarks are drawn in Section 5. Appendix A gives mathematical details of the inertial benchmark used in Section 4.

2. Solid, Fluid and Interaction Problem Formulations and Discretizations

This section provides an overview of the equations governing the FSI problem. We adopt a Lagrangian specification of the immersed structure and a

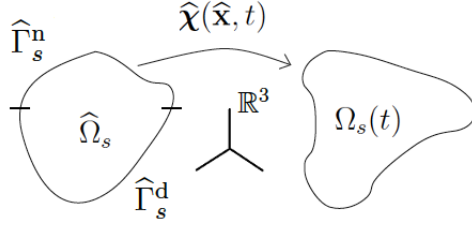


Figure 1: Reference configuration (left) and current configuration (right) of a continuum body. Here the boundary $\partial\hat{\Omega}_s$ is split into nonoverlapping Neumann $\hat{\Gamma}_s^n$ and Dirichlet $\hat{\Gamma}_s^d$ boundaries.

Eulerian specification of the fluid.

2.1. Solid Dynamics Formulation

Let $\hat{\Omega}_s \subset \mathbb{R}^3$ be a bounded Lipschitz domain. We refer to a body of mass undergoing a motion from the material (reference) configuration, $\hat{\Omega}_s$, to the current (spatial) configuration, $\Omega_s(t)$ (Figure 1). The material position $\hat{\mathbf{x}}$ and the actual position \mathbf{x} are linked during the time interval $I := [0, T]$ of interest by a one-to-one mapping, called *motion* $\hat{\chi} : \hat{\Omega}_s \times I \rightarrow \mathbb{R}^d$, with spatial dimension $d \in \{1, 2, 3\}$ such that $\mathbf{x} = \hat{\chi}(\hat{\mathbf{x}}, t)$, $\forall t \in I$.

Governing Equations. As customary in solid dynamics, the solid subproblem is described in terms of the mapping $\hat{\chi}$. The total Lagrangian specification of the elastodynamics balance equations for the solid domain is:

$$\hat{\rho}_s \frac{\partial^2 \hat{\mathbf{u}}_s}{\partial t^2} - \hat{\nabla} \cdot \hat{\mathbf{P}} = \mathbf{0} \quad \text{on} \quad \hat{\Omega}_s. \quad (1)$$

Here $\hat{\rho}_s$ is the mass density per unit undeformed volume, $\hat{\mathbf{u}}_s = \hat{\mathbf{u}}_s(\hat{\mathbf{x}}, t)$ is the displacement field, $\hat{\mathbf{P}} = \hat{\mathbf{P}}(\hat{\mathbf{x}}, t)$ is the first Piola–Kirchhoff stress tensor, and $\hat{\nabla} \cdot$ is the divergence operator computed in the reference configuration.

For a hyperelastic material the first Piola–Kirchhoff stress tensor $\hat{\mathbf{P}} = \partial\Psi/\partial\mathbf{F}$ is related to the deformation through a constitutive equation derived from a given scalar energy function Ψ . In this paper we will consider the Saint-Venant–Kirchhoff constitutive relation, Ψ_I , and the fiber-reinforced model proposed by

Holzappel [26], Ψ_{II} , which read as follows:

$$\Psi_I = \frac{\lambda}{2} [\text{tr}(\widehat{\mathbf{E}})]^2 + \mu_s \text{tr}(\widehat{\mathbf{E}}^2), \quad (2)$$

$$\Psi_{II} = \mu_s (\bar{I}_1 - 3) + \frac{k_{11}}{2k_{21}} (\exp[k_{21}(\bar{I}_{4,1} - 1)^2] - 1) + \frac{k_{12}}{2k_{22}} (\exp[k_{22}(\bar{I}_{4,2} - 1)^2] - 1). \quad (3)$$

Here $\widehat{\mathbf{E}} = (\widehat{\mathbf{F}}^T \widehat{\mathbf{F}} - \mathbf{I})/2$ is the Green-Lagrangian strain tensor, $\text{tr}(\cdot)$ is the trace operator, λ_s , μ_s and k_{ij} are the constitutive parameters, and \bar{I}_1 , $\bar{I}_{4,1}$ and $\bar{I}_{4,2}$, are modified invariants defined as

$$\bar{I}_1 = \widehat{J}^{-2/3} \text{tr}(\widehat{\mathbf{C}}) \quad \bar{I}_{4,1} = \widehat{J}^{-2/3} \mathbf{g}_{0,1} \cdot \widehat{\mathbf{C}} \mathbf{g}_{0,1} \quad \bar{I}_{4,2} = \widehat{J}^{-2/3} \mathbf{g}_{0,2} \cdot \widehat{\mathbf{C}} \mathbf{g}_{0,2}, \quad (4)$$

with the unit vectors $\mathbf{g}_{0,1}$ and $\mathbf{g}_{0,2}$ denoting the fiber orientation, $\widehat{J} := \det(\widehat{\mathbf{F}})$ being the determinant of the deformation gradient tensor and $\widehat{\mathbf{C}} := \widehat{\mathbf{F}}^T \widehat{\mathbf{F}}$ being the right Cauchy–Green strain tensor.

In order to fulfill the incompressibility condition, the penalty technique is employed. In this method, a volumetric energy term $\Psi_V(J) = 1/2\kappa(J - 1)^2$ is added to the expression of the strain energy function Ψ with κ representing the penalty coefficient.

Equation (1) must be supplied with initial conditions for the displacement field and the velocity field:

$$\begin{aligned} \widehat{\mathbf{u}}_s(\cdot, 0) &= \widehat{\mathbf{u}}_{s0} \quad \text{on } \widehat{\Omega}_s, \\ \frac{\partial \widehat{\mathbf{u}}_s(\cdot, 0)}{\partial t} &= \widehat{\mathbf{v}}_{s0} \quad \text{on } \widehat{\Omega}_s, \end{aligned} \quad (5)$$

where $\widehat{\mathbf{u}}_{s0}$ and $\widehat{\mathbf{v}}_{s0}$ are given initial data, and with suitable boundary conditions. After splitting the boundary $\partial \widehat{\Omega}_s$ into the Neumann $\widehat{\Gamma}_s^n$ and the Dirichlet $\widehat{\Gamma}_s^d$ nonoverlapping parts (Figure 1), the following boundary conditions are considered:

$$\begin{aligned} \widehat{\mathbf{u}}_s &= \widehat{\mathbf{b}} \quad \text{on } \widehat{\Gamma}_s^d, \\ \widehat{\mathbf{P}} \cdot \widehat{\mathbf{n}}_s &= \mathbf{0} \quad \text{on } \widehat{\Gamma}_s^n, \end{aligned} \quad (6)$$

where $\widehat{\mathbf{n}}_s$ is the outward normal and $\widehat{\mathbf{b}}$ is a prescribed boundary datum.

Weak Formulation. Introducing the space of admissible test functions as

$$\widehat{\mathbf{V}}_s = \{\phi_s \in \mathbf{H}^1(\widehat{\Omega}_s) : \phi_s|_{\widehat{\Gamma}_s^d} = \mathbf{0}\},$$

where $\mathbf{H}^1(\widehat{\Omega}_s)$ is the Sobolev space of weakly differentiable functions, the weak formulation of the elastodynamics balance equations (1) reads:

$$\int_{\widehat{\Omega}_s} \widehat{\rho}_{s0} \frac{\partial^2 \widehat{\mathbf{u}}_s}{\partial t^2} \cdot \phi_s \, d\widehat{V} + \int_{\widehat{\Omega}_s} \widehat{\mathbf{P}} : \widehat{\nabla} \phi_s \, d\widehat{V} = \mathbf{0} \quad \forall \phi_s \in \widehat{\mathbf{V}}_s. \quad (7)$$

Spatial Discretization. We assume that the solid domain $\widehat{\Omega}_s$ can be approximated by a discrete domain $\widehat{\Omega}_s^h$ and the associated mesh $\widehat{T}_s^h = \{\widehat{E}_s \subseteq \widehat{\Omega}_s^h \mid \bigcup \widehat{E}_s = \widehat{\Omega}_s^h\}$, where its elements \widehat{E}_s form a partition; hence for $E_s^1, E_s^2 \subseteq \widehat{T}_s^h$ and $E_s^1 \neq E_s^2$, then $E_s^1 \cap E_s^2 = \emptyset$.

For the spatial discretization, we consider first-order finite elements for which the corresponding function space is defined as

$$\widehat{X}_s^h(\widehat{T}_s^h) = \{\phi_s^h \in C^0(\widehat{\Omega}_s^h), \phi_s^h|_{\widehat{E}_s} \in \mathbb{P}_1 \, \forall \widehat{E}_s \in \widehat{T}_s^h\},$$

where \mathbb{P}_1 is the space of linear polynomials defined on each element $\widehat{E}_s \in \widehat{T}_s^h$.

Hence, the Galerkin formulation of the solid subproblem (7) reads:

$$\int_{\widehat{\Omega}_s} \widehat{\rho}_s \frac{\partial^2 \widehat{\mathbf{u}}_s^h}{\partial t^2} \cdot \phi_s^h \, d\widehat{V} + \int_{\widehat{\Omega}_s} \widehat{\mathbf{P}}(\widehat{\mathbf{u}}_s^h) : \widehat{\nabla} \phi_s^h \, d\widehat{V} = \mathbf{0} \quad \forall \phi_s^h \in \widehat{\mathbf{V}}_s^h. \quad (8)$$

Let $\{\mathbf{N}_{s,i}^h\}_{i \in J_s}$ be the Lagrangian basis of the space $\widehat{\mathbf{V}}_s^h := \widehat{\mathbf{V}}_s \cap \widehat{X}_s^h$ where $J_s \subset \mathbb{N}$ is an index set, then the problem (8) can be written as:

$$\widehat{\rho}_s \mathbf{M} \frac{\partial^2 \widehat{\mathbf{u}}_s}{\partial t^2} + \mathbf{K}(\widehat{\mathbf{u}}_s) = \mathbf{0}. \quad (9)$$

where $\widehat{\mathbf{u}}_s = [\widehat{u}_{s,i}]$ is the vector of the unknowns of the problem, \mathbf{M} is the mass matrix and \mathbf{K} is the vector of nonlinear internal forces defined as follows:

$$\begin{aligned} \mathbf{M}_{ij} &= \int_{\widehat{\Omega}_s} \mathbf{N}_{s,j}^h \cdot \mathbf{N}_{s,i}^h \, d\widehat{V}, \\ \mathbf{K}(\widehat{\mathbf{u}}_s)_i &= \int_{\widehat{\Omega}_s} \widehat{\mathbf{P}}(\widehat{\mathbf{u}}_s) : \widehat{\nabla} \mathbf{N}_{s,i}^h \, d\widehat{V}. \end{aligned}$$

Time Discretization. The Newmark scheme [27, 28] is adopted for the temporal discretization of the solid subproblem. Hence the discretized equation of motion (1) for a given discrete time step n reads:

$$\hat{\rho}_s \mathbf{M} \frac{\hat{\mathbf{u}}_s^{n+1}}{\Delta t^2} + \beta \mathbf{K}(\hat{\mathbf{u}}_s^{n+1}) = \beta \mathbf{F}^n, \quad (10)$$

with

$$\mathbf{F}^n := \hat{\rho}_s \mathbf{M} \frac{\hat{\mathbf{u}}_s^n}{\Delta t^2} + \hat{\rho}_s \mathbf{M} \frac{\hat{\mathbf{v}}_s^n}{\Delta t} + \hat{\rho}_s \mathbf{M} \frac{(1-2\beta)}{2} \hat{\mathbf{a}}_s^n.$$

Equation (10) together with the following approximations:

$$\hat{\mathbf{u}}_s^{n+1} = \hat{\mathbf{u}}_s^n + \Delta t \hat{\mathbf{v}}_s^n + \frac{\Delta t^2}{2} (2\beta \hat{\mathbf{a}}_s^{n+1} + (1-2\beta) \hat{\mathbf{a}}_s^n) \quad (11)$$

$$\hat{\mathbf{v}}_s^{n+1} = \hat{\mathbf{v}}_s^n + \Delta t ((1-\gamma) \hat{\mathbf{a}}_s^n + \gamma \hat{\mathbf{a}}_s^{n+1}) \quad (12)$$

defines the Newmark scheme. Here $\hat{\mathbf{a}}_s = \partial^2 \hat{\mathbf{u}}_s / \partial t^2$ and $\hat{\mathbf{v}}_s = \partial \hat{\mathbf{u}}_s / \partial t$ denote the acceleration and velocity fields of the structure, respectively; β and γ are real parameters used to control the amplification of the high frequency modes which are not of interest. In the numerical experiments presented in Section 4, we adopt the following set of parameters: $\beta = 0.25$ and $\gamma = 0.50$.

Implementation. The solid subproblem is implemented in the finite element framework MOOSE (<https://www.mooseframework.org>). A Newton method is used for solving the solid subproblem, whereas the MULTifrontal Massively Parallel Sparse direct Solver (MUMPS) is employed for solving the associated linear system.

2.2. Fluid Dynamics Formulation

The fluid dynamics subproblem is formulated in an Eulerian specification where a bounded domain Ω_f is considered.

Governing Equations. In the domain Ω_f , the Navier–Stokes equations for incompressible flow in nondimensional form are

$$\frac{\partial \tilde{\mathbf{v}}_f}{\partial t} + (\tilde{\mathbf{v}}_f \cdot \tilde{\nabla}) \tilde{\mathbf{v}}_f + \tilde{\nabla} \tilde{p}_f - \frac{1}{\text{Re}} \tilde{\Delta} \tilde{\mathbf{v}}_f = \tilde{\mathbf{f}}, \quad (13a)$$

$$\tilde{\nabla} \cdot \tilde{\mathbf{v}}_f = 0, \quad (13b)$$

where the dimensional quantities have been nondimensionalized according to:

$$\begin{aligned} \mathbf{v}_f &= \tilde{\mathbf{v}}_f U_{\text{ref}}, & \mathbf{x} &= \tilde{\mathbf{x}} L_{\text{ref}}, & t &= \tilde{t} L_{\text{ref}} / U_{\text{ref}}, \\ p_f &= \tilde{p}_f \rho_f U_{\text{ref}}^2, & \mathbf{f} &= \tilde{\mathbf{f}} \rho_f U_{\text{ref}}^2 / L_{\text{ref}}, & \text{Re} &= \rho_f U_{\text{ref}} L_{\text{ref}} / \mu_f. \end{aligned}$$

Here, \mathbf{v}_f is the fluid velocity vector field, \mathbf{x} is the coordinate vector with components $x_{1,2,3}$, p_f is the fluid pressure, \mathbf{f} is an external force density; ρ_f , μ_f , L_{ref} and U_{ref} are the fluid density, dynamic viscosity, reference length and reference velocity, respectively; $\text{Re} := \rho_f U_{\text{ref}} L_{\text{ref}} / \mu_f$ is the Reynolds number.

We introduce the notations \mathcal{D} for the divergence operator, $\mathcal{L}\tilde{\mathbf{v}}_f$ for the linear viscous term, $\mathcal{G}\tilde{p}_f$ for the pressure gradient and \mathcal{N} for all other terms in Equation (13a) except the temporal derivative. As such the Navier–Stokes equations can be written in matrix operator form as:

$$\frac{\partial}{\partial \tilde{t}} \begin{bmatrix} \tilde{\mathbf{v}}_f \\ 0 \end{bmatrix} + \begin{bmatrix} -\mathcal{L} & \mathcal{G} \\ \mathcal{D} & 0 \end{bmatrix} \begin{bmatrix} \tilde{\mathbf{v}}_f \\ \tilde{p}_f \end{bmatrix} = \begin{bmatrix} \mathcal{N}(\tilde{\mathbf{v}}_f, \tilde{\mathbf{f}}) \\ 0 \end{bmatrix}. \quad (14)$$

Time Discretization. Although our framework allows also for a semi-implicit time integration scheme, an explicit low-storage third-order three-stage Runge–Kutta method [29] is adopted for the time discretization of the fluid subproblem. Because the source force term in the FSI formulation (see Section 2.3) imposes a time step restriction which is more stringent than the CFL-like (Courant–Friedrichs–Lewy) stability condition arising from the viscous term [30], the computational cost of an implicit treatment of the viscous term cannot be justified by a larger time step size.

The use of the explicit time integrator leads to a coupled system of linear equations for the velocity $\tilde{\mathbf{v}}_f^{(m)}$ and the pressure $\tilde{p}_f^{(m)}$ at the subtime step $m = \{1, 2, 3\}$ which reads:

$$\begin{bmatrix} \mathcal{I} & c_m \Delta \tilde{t} \mathcal{G} \\ \mathcal{D} & 0 \end{bmatrix} \begin{bmatrix} \tilde{\mathbf{v}}_f^{(m)} \\ \tilde{p}_f^{(m)} \end{bmatrix} = \begin{bmatrix} q(\tilde{\mathbf{v}}_f^{(m-1)}, \tilde{\mathbf{v}}_f^{(m-2)}, \tilde{\mathbf{f}}) \\ \mathbf{0} \end{bmatrix}, \quad (15)$$

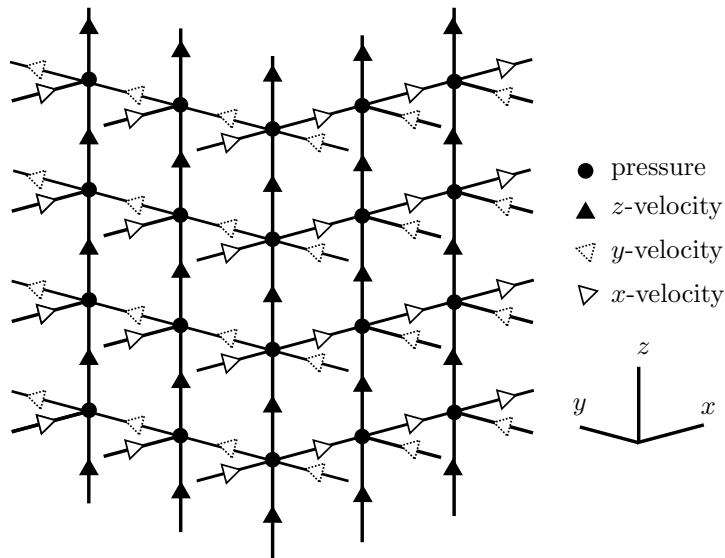


Figure 2: Three-dimensional staggered grid adopted for the fluid subproblem.

where \mathcal{I} is an identity matrix, q contains the right-hand side arising from the low storage Runge–Kutta scheme and c_m is the Runge–Kutta stage coefficient.

Spatial Discretization. We use finite differences of high convergence order (sixth-order) on a rectilinear structured grid for the spatial discretization of Equation (15) [31]. This leads to a linear system of equations of the form:

$$\begin{bmatrix} \mathbf{J} & \mathbf{G} \\ \mathbf{D} & \mathbf{0} \end{bmatrix} \begin{bmatrix} \tilde{\mathbf{v}}_f \\ \tilde{\mathbf{p}}_f \end{bmatrix} = \begin{bmatrix} \mathbf{q} \\ \mathbf{0} \end{bmatrix} \quad (16)$$

Here the matrices \mathbf{D} and \mathbf{G} are the spatial discretization of the operators \mathcal{D} and \mathcal{G} , respectively, \mathbf{q} is the discrete representation of the right-hand side q and the discrete identity matrix \mathbf{J} also contains the values of the velocity boundary conditions. We work with four subgrids, one for each velocity component and one for the pressure (Figure 2). The momentum equations are solved on the respective velocity grids, which implies that the discrete operator \mathbf{G} requires

the evaluation of the first derivatives of the velocity grids 1, 2, 3 from values on the grid 0. The continuity equation is satisfied on the pressure grid, i.e. the discrete operator \mathbf{D} computes the first derivative on the pressure grid 0 from the values of the grids 1, 2, 3.

We can derive an equation for the pressure by forming the Schur complement of Equation (16):

$$\mathbf{D}\mathbf{J}^{-1}\mathbf{G}\tilde{\mathbf{p}}_f = \mathbf{D}\mathbf{J}^{-1}\mathbf{q}. \quad (17)$$

The Poisson problem (17) is solved with the iterative Krylov subspace method BiCGstab with right preconditioning by a V -cycle geometric multigrid preconditioner of Gauss–Seidel type [31]. To aid convergence we compute the left null-space of the pressure operator and project it onto the column space of the operator as described in [31, 32].

Implementation. The described numerical approach is implemented in the Navier–Stokes solver IMPACT which is thoroughly validated and has been used for several complex flow configurations [33, 34, 35]. More details on this solver can be found in [31].

2.3. Fluid-Structure Coupling

The coupling between the discretizations of the fluid and the solid sub-problems is established by enforcing congruent velocities at the interface Γ^{fsi} between fluid and structure (Figure 3) and by adding a force density term to the Navier–Stokes equations to account for the immersed solid structure. The strong formulation of the FSI problem reads as follows:

$$\hat{\rho}_s \frac{\partial^2 \hat{\mathbf{u}}_s}{\partial t^2} - \hat{\nabla} \cdot \hat{\mathbf{P}} = \mathbf{0} \quad \text{in } \hat{\Omega}_s \quad (18a)$$

$$\frac{\partial \tilde{\mathbf{v}}_f}{\partial t} + (\tilde{\mathbf{v}}_f \cdot \tilde{\nabla}) \tilde{\mathbf{v}}_f + \tilde{\nabla} \tilde{p}_f - \frac{1}{\text{Re}} \tilde{\Delta} \tilde{\mathbf{v}}_f = \tilde{\mathbf{f}}_{\text{fsi}} \quad \text{in } \Omega_f \quad (18b)$$

$$\tilde{\nabla} \cdot \tilde{\mathbf{v}}_f = 0 \quad \text{in } \Omega_f \quad (18c)$$

$$\frac{\partial \mathbf{u}_s}{\partial t} = \mathbf{v}_f \quad \text{on } \Gamma^{\text{fsi}} \quad (18d)$$

$$\mathbf{v}_f = \mathbf{v}_b \quad \text{on } \partial\Omega_f \quad (18e)$$

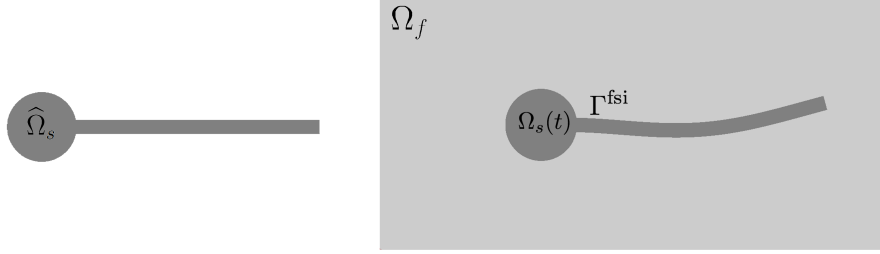


Figure 3: (Left) Reference configuration of the solid domain ($\hat{\Omega}_s$). (Right) Eulerian representation of the fluid domain (Ω_f) in which the current configuration of the structure ($\Omega_s(t)$) is immersed. Γ^{fsi} represents the boundary of fluid-structure interaction.

where $\partial\Omega_f$ is the boundary of the fluid domain and $\mathbf{f}_{\text{fsi}} = \tilde{\mathbf{f}}_{\text{fsi}}\rho_f U_{\text{ref}}^2/L_{\text{ref}}$ is the reaction force density generated by the immersed solid. It is computed as:

$$\int_{\hat{\Omega}_s} \mathbf{f}_{\text{fsi}} \cdot \boldsymbol{\phi}_s d\hat{V} = \int_{\hat{\Omega}_s} \hat{\rho}_s \frac{\partial^2 \hat{\mathbf{u}}_s}{\partial t^2} \cdot \boldsymbol{\phi}_s d\hat{V} + \int_{\hat{\Omega}_s} \hat{\mathbf{P}} : \hat{\nabla} \boldsymbol{\phi}_s d\hat{V}. \quad (19)$$

Equations (18) are supplied with initial conditions for the displacement and velocity field of the solid structure and for the velocity field of the fluid domain:

$$\hat{\mathbf{u}}_s(\mathbf{x}, 0) = \hat{\mathbf{u}}_s^0 \quad \text{in } \hat{\Omega}_s \quad (20)$$

$$\frac{\partial \hat{\mathbf{u}}_s}{\partial t}(\mathbf{x}, 0) = \frac{\partial \hat{\mathbf{u}}_s^0}{\partial t} \quad \text{in } \hat{\Omega}_s \quad (21)$$

$$\mathbf{v}_f(\mathbf{x}, 0) = \mathbf{v}_f^0 \quad \text{in } \Omega_f \quad (22)$$

Variational Transfer: the L^2 -Projection Approach. The coupling between fluid and structure requires the transfer of the velocities \mathbf{v}_f and the force density \mathbf{f}_{fsi} from the Eulerian fluid grid to the Lagrangian solid mesh and vice versa (Figure 4).

In the classical IBM, the coupling between the two types of variables involves a smoothed approximation of the Dirac-delta function. It is well known that such an approach can suffer from poor volume conservation [2, 3]. This manifests itself as an apparent fluid *leak* at fluid-structure interfaces, which occurs even though the Lagrangian structure moves at the local fluid velocity. This leaking

can be observed as a numerical artifact that appears when the fluid element size is much smaller than that of the structure. A heuristic estimation of mesh ratio of two is recommended to prevent leaking [36].

In this work, the finite difference discretization of the fluid dynamics subproblem and the finite element discretization of the solid dynamics subproblem are coupled by means of L^2 -projections. This coupling approach allows for the transfer of discrete fields between unstructured and structured discretized domains in a transparent, efficient, and flexible way.

The use of the L^2 -projection approach requires to attach Lagrangian basis functions to the finite difference grid [37], and to define the corresponding auxiliary finite element space as $\mathbf{V}_f^h = \mathbf{V}_f^h(T_f^h) \subset [H_0^1(\Omega_f)]^d$ where T_f^h indicates the fluid grid (Figure 4). Further, we introduce a suitable discrete space of Lagrangian multipliers $\mathbf{M}_{\text{fsi}}^h(T_s^h)$, where T_s^h represents the current configuration of the solid mesh.

We introduce the FSI projection operator $\Pi : V_f^h \rightarrow V_s^h$ for the transfer of the discrete velocity field from the fluid grid to the solid mesh. For each scalar component of the velocity $v_f^h \in V_f^h$ we want to find $w_s^h = \Pi(v_f^h) \in V_s^h$, such that:

$$\int_{I_h} (v_f^h - \Pi(v_f^h)) \lambda_{\text{fsi}}^h dV = \int_{I_h} (v_f^h - w_s^h) \lambda_{\text{fsi}}^h = 0 dV \quad \forall \lambda_{\text{fsi}}^h \in M_{\text{fsi}}^h. \quad (23)$$

where I_h denotes the overlapping region between fluid grid and structure mesh, $I_h := T_s^h \cap T_f^h$, here coinciding with the solid mesh T_s^h . Let $\{N_{f,i}^h\}_{i \in J_f}$ and $\{N_{\text{fsi},i}^h\}_{i \in J_{\text{fsi}}}$ be the Lagrangian basis functions of the spaces \mathbf{V}_f^h and $\mathbf{M}_{\text{fsi}}^h$, respectively, with $J_f \in \mathbb{N}$ and $J_{\text{fsi}} \in \mathbb{N}$ suitable index sets, then we get the so-called mortar integrals:

$$\mathbf{B}_{ij} = \int_{I_h} N_{f,j}^h N_{\text{fsi},i}^h dV \quad \mathbf{S}_{ij} = \int_{I_h} N_{s,j}^h N_{\text{fsi},i}^h dV. \quad (24)$$

Equation (23) can be written in algebraic form:

$$\mathbf{B}\mathbf{v}_f = \mathbf{S}\mathbf{w}_s \quad (25)$$

where \mathbf{w}_s and \mathbf{v}_f are vectors of coefficients entries $w_s^{h,i}$ and $v_f^{h,i}$. In the present

case \mathbf{S} is square-shaped, thus one may compute the transfer operator \mathbf{T} as:

$$\mathbf{w}_s = \mathbf{S}^{-1} \mathbf{B} \mathbf{v}_f = \mathbf{T} \mathbf{v}_f \quad (26)$$

To reduce the computational cost required to compute the inverse of the matrix \mathbf{S} , dual basis functions may be adopted for the functional space M_{fsi}^h . In this case the functional space is spanned by a set of functions which are biorthogonal to the basis functions of V_s^h with respect to the L^2 inner product:

$$(N_{j,s}^h, N_{k,\text{fsi}}^h)_{L^2(I^h)} = \delta_{j,k} (N_{k,\text{fsi}}^h, 1)_{L^2(I^h)} \quad \forall i, j \quad (27)$$

The usage of the dual basis functions corresponds to replacing the standard L^2 -projection with the local approximation (Equation (27)) which we call ‘pseudo’ L^2 -projection. This choice allows for a more efficient evaluation of the transfer operator \mathbf{T} since the matrix \mathbf{S} becomes diagonal. Finally, we use the transpose operator \mathbf{T}^T to transfer the reaction forces from the solid mesh to the fluid grid:

$$\tilde{\mathbf{f}}_{\text{fsi}} = L_{\text{ref}} / (\rho_f U_{\text{ref}}^2) \mathbf{T}^T \mathbf{f}_{\text{fsi}}. \quad (28)$$

Here $\tilde{\mathbf{f}}_{\text{fsi}}$ is obtained by making nondimensional the L^2 -projection of the vector $\mathbf{f}_{\text{fsi}} \in \mathbf{V}_s^h(T_s^h)$ corresponding to the reaction force \mathbf{f}_{fsi} defined in Equation (19).

The transfer operator is assembled as follows: (I) detect the overlapping region by means of a tree-search algorithm, (II) generate the quadrature points for integrating in the intersecting region, (III) compute the local element-wise contributions for the operators \mathbf{B} and \mathbf{S} by means of numerical quadrature rules and (IV) finally assemble the two mortar matrices. The current implementation of the procedure described in [24] generates quadrature points exclusively for piecewise affine meshes. The necessity of transferring data in the current configuration of the solid mesh T_s^h motivates the choice of \mathbb{P}_1 elements for the discretization of solid subproblem.

Remark. *In the classical IBM, the evaluation of the dynamic terms in the solid structure in Equation (18a) is carried out using the difference between the solid and the fluid densities $\hat{\rho}_s - \rho_f$ [22]. Here, this difference in density is only*

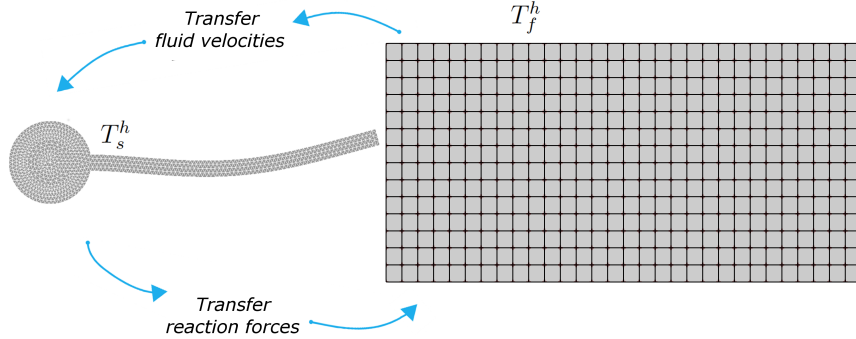


Figure 4: Schematic representation of the coupling strategy. Deformed solid mesh, T_s^h , on the left and fluid grid, T_f^h , on the right.

applied to the boundary Γ^{fsi} , because we enforce the displacement from the flow field only on the boundary Γ^{fsi} . Further, we choose not to eliminate the fluid stress terms at the interface with the solid domains from the Navier–Stokes equations (Equation (18b)), because the fluid stresses are typically considered negligible compared to the solid stresses imposed on the interface Γ^{fsi} [22].

3. Fluid-Structure Interaction algorithm

For solving the discretized FSI problem we adopt a segregated approach with a fixed point (Picard) iteration at each time step. To ensure numerical stability in time of the coupled nonlinear FSI system (Figure 5), the system is solved to a sufficient spatial accuracy in each time step.

For a given time step n and given a starting solution at the Picard iteration $p = l$ with $l \in \mathbb{N}$, the FSI algorithm determines the solution at the next time step $n + 1$ as follows:

Step 1: Transfer the fluid velocity from the fluid grid to the current configuration of the solid mesh.

$$\mathbf{w}_{s,l} = \mathbf{T}\mathbf{v}_{f,l-1} \quad (29)$$

Step 2: Compute the displacement field of the solid structure on the interface Γ_{fsi} and use it as a boundary condition for the elastodynamics equations (9).

$$\hat{\mathbf{u}}_{s,l} = \hat{\mathbf{u}}_{s,0} + \Delta t \mathbf{w}_{s,l} \quad (30)$$

Step 3: Solve the elastodynamics equations (9) and compute the reaction force $\mathbf{f}_{\text{fsi},l}$.

Step 4: Transfer the reaction force $\mathbf{f}_{\text{fsi},l}$ from the current configuration of the solid mesh to the fluid grid.

$$\tilde{\mathbf{f}}_{\text{fsi},l} = L_{\text{ref}} / (\rho_f U_{\text{ref}}^2) \mathbf{T}^T \mathbf{f}_{\text{fsi},l} \quad (31)$$

Step 5: Solve the Navier–Stokes equations (18b),(18c) by using the force $\tilde{\mathbf{f}}_{\text{fsi},l}$ as source term to get the new velocity value $\mathbf{v}_{f,l}$.

Step 6: Compute residual norms of the difference between the two latest available sets of FSI force terms and compare them with a given threshold as follows:

Absolute convergence criterion

$$\|\mathbf{f}_{\text{fsi},l} - \mathbf{f}_{\text{fsi},l-1}\|_{\infty} < \epsilon_A \quad (32)$$

Relative convergence criterion

$$\frac{\|\mathbf{f}_{\text{fsi},l} - \mathbf{f}_{\text{fsi},l-1}\|_{\infty}}{\|\mathbf{f}_{0,\text{fsi}}\|} < \epsilon_R \quad (33)$$

Start a new Picard iteration if neither of these conditions are satisfied.

Advance to a new time step if one of the two criteria is satisfied.

Implementation. The FSI algorithm is implemented in the finite element framework MOOSE and includes an interface with the library MOONoLith (https://bitbucket.org/zulianp/par_moonolith) and the flow solver IMPACT.

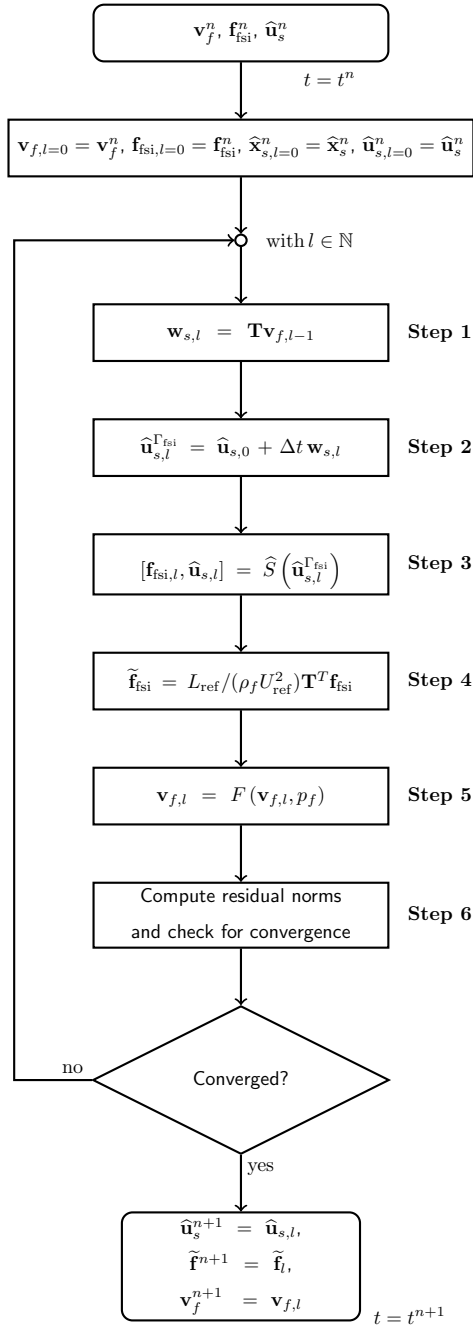


Figure 5: Flow chart of the FSI algorithm. Here \widehat{S} is the solid subproblem and F is the fluid subproblem.

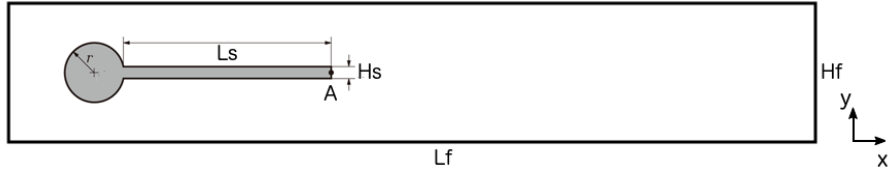


Figure 6: Geometry of the Turek–Hron benchmark.

4. Numerical Results

A series of numerical simulations are presented in order to demonstrate the accuracy, robustness and flexibility of the developed computational framework. We present examples for moderately high Reynolds numbers. All computations have been performed on the *Piz Daint* supercomputer at CSCS (Lugano, Switzerland), a hybrid Cray XC40/XC50 system with a total of 5320 hybrid (GPU/CPU) compute nodes equipped with a 12-core 64-bit Intel Haswell CPU (Intel Xeon E5-2690 v3), an NVIDIA Tesla P100 with 64 GB of hybrid memory.

4.1. Turek–Hron FSI benchmark

In this section, we present results for the Turek–Hron FSI benchmark [38] of an incompressible flow past an elastic solid structure.

The fluid domain (Figure 6) has a length of $L_f = 3$ [m] and height $H_f = 0.41$ [m], whereas the immersed solid structure is composed of a disk with radius $r = 0.05$ [m] centered at $C = (0.2$ [m], 0.2 [m]) (measured from the left bottom corner of the channel) and a tail consisting of a rectangular elastic beam of length $L_s = 0.35$ [m] and height $H_s = 0.02$ [m]; its right bottom corner is positioned at $(0.6$ [m], 0.19 [m]), and the left end is fixed to the circle. The fluid domain is discretized using a Cartesian grid with 769×129 grid points which is stretched to concentrate points around the structure. The solid mesh consists of 3273 linear finite elements (\mathbb{P}_1) with 1791 nodes. Bilinear finite elements (\mathbb{Q}_1) are used for the auxiliary function space \mathbf{V}_f^h associated with the fluid subproblem for the assembly of the transfer operator \mathbf{T} .

Periodic boundary conditions are imposed at the inlet and outlet of the fluid channel together with no-slip boundary conditions on the top and the bottom.

A parabolic velocity profile $\mathbf{v}_0(\mathbf{x}, t)$

$$\mathbf{v}_0 = 1.5 U_{\text{ref}} \frac{y(H_f - y)}{H_f^2/4}, \quad (34)$$

is enforced upstream of the structure by adding a fringe forcing term [39] to the right-hand side of the Navier–Stokes equations. The fringe force acts in the region $x_{\text{start}} < x < x_{\text{end}}$ and is defined by the function $\lambda(x)$:

$$\lambda(x) = \hat{\lambda} \left[S \left(\frac{x - x_{\text{start}}}{d_{\text{rise}}} \right) - S \left(\frac{x - x_{\text{end}}}{d_{\text{fall}}} + 1 \right) \right], \quad (35)$$

and

$$S(x) = \begin{cases} 0, & x \leq 0; \\ \left(1 + \exp \left(\frac{1}{1-x} + \frac{1}{x} \right) \right)^{-1} & 0 < x < 1; \\ 1, & x \geq 1, \end{cases} \quad (36)$$

with $x_{\text{start}} = 2.5$, $x_{\text{end}} = 3.0$, $d_{\text{rise}} = d_{\text{fall}} = 0.025$ and $\hat{\lambda} = 10$. In this region we enforce the velocity profile $\mathbf{v}_0 = U_{\text{ref}} \tilde{\mathbf{v}}_0$ and an appropriate fluid pressure increase by

$$\tilde{\mathbf{f}}_{\text{fringe}} = \lambda(\tilde{x}) \left[(\tilde{\mathbf{v}}_0 - \tilde{\mathbf{v}}_f) + \frac{\tilde{L}_f}{\hat{\lambda}(\tilde{x}_{\text{end}} - \tilde{x}_{\text{start}})} \cdot \frac{8}{\tilde{H}_f^2 \text{Re}} \right]. \quad (37)$$

We performed tests for two parameter sets (Table 1). Set I corresponds to the FSI3 benchmark in [38]. It has matching fluid and solid densities and we employ a Saint-Venant–Kirchhoff material model. Set II uses different material properties for the circle and the rectangular tail. This last numerical example demonstrates that our FSI framework can also handle non homogenous material properties for the solid structure.

Figure 7 illustrates the temporal evolution of the vorticity field at different points in time. The effect of the fringe forcing can be observed at the downstream end of the computational domain: the vortices are damped out and the Poiseuille flow is re-established.

Figure 8a shows the displacements in x - and y -direction of a control point $A = (0.6 \text{ [m]}, 0.2 \text{ [m]})$ located at the end of the elastic tail (Figure 6). The quantities of interest were fitted with a sinusoidal function of the form $[A \cdot$

Table 1: Parameters of Turek–Hron runs

parameters	I (FSI3)	II
ρ_s [kg/m ³]	1000	1000
μ_s [MPa]	0.5	circle: 2, tail: 0.1
λ_s [MPa]	4.67	circle: 4.67, tail: 0.23
ρ_f [kg/m ³]	1000	1000
μ_f [Pa · s]	1	1
U_{ref} [m/s]	2	2

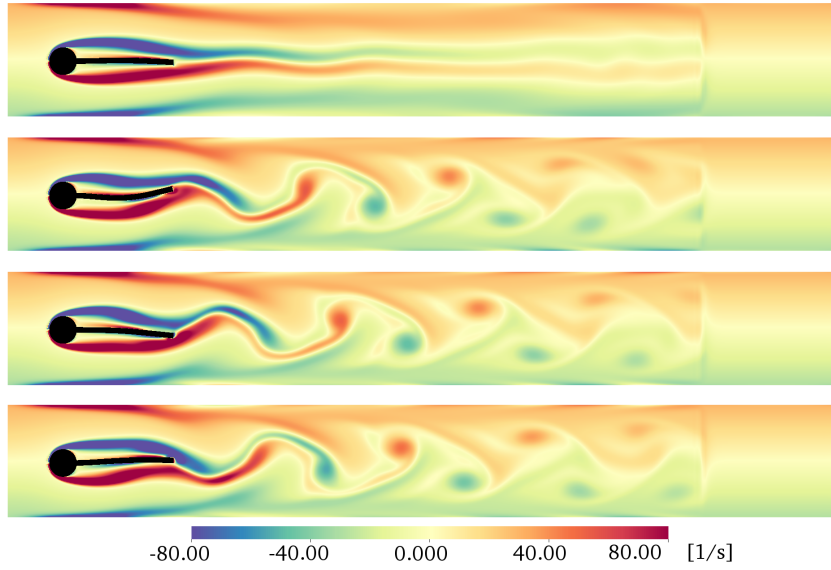


Figure 7: Fluid vorticity [1/s] at times $t = 1.34, 2.77, 5.50, 19.17$ [s] for parameter set I. Times correspond to snapshots at 7, 14.5, 28.75 and 100.25 steady-state periods.

$\sin(2\pi \cdot f \cdot t + \phi) + M]$ and the retrieved values can be found in Table 2. The mean vertical displacement M is 0.00137 with amplitude $A = \pm 0.0338$ [m] and the horizontal displacement is -0.00255 ± 0.00231 [m]; the frequency f of the y -displacement $u_{s,y}$ is 5.23 [Hz], and the frequency f for the x -displacement $u_{s,x}$ is about 10.45 [Hz]. The drag and lift forces on the structure over time are presented in Figure 8b and their values can be found in Table 2. All quantities agree well with the results obtained with other numerical methods applied to the same problem [38].

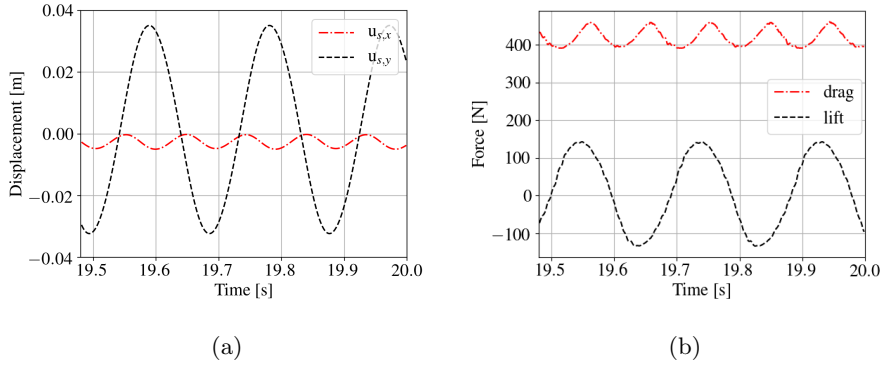


Figure 8: (a) Displacements of control point A located at the end of the elastic beam and (b) lift and drag forces for parameter set I (Table 1).

We further consider another set of parameters (set II, Table 1) with inhomogeneous mechanical properties for the circle (C) and the rectangular tail (T) of the solid beam. The results in Figure 9a show an amplitude A of 0.0513 [m] for the vertical displacement and of 0.00707 [m] for the mean horizontal displacement. Moreover, the frequency f is 6.27 [Hz] for the y -displacement $u_{s,y}$ and 12.54 [Hz] for the x -displacement $u_{s,x}$. Lift and drag forces are visualized in Figure 9b, and the corresponding quantities of interest, i.e. amplitude and frequency, can be found in Table 2.

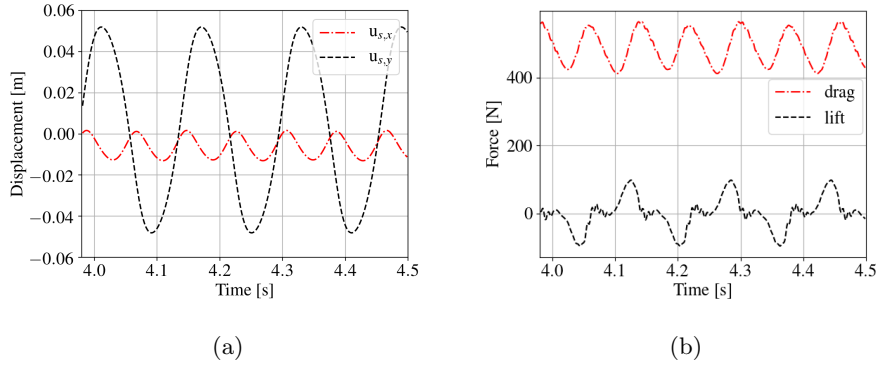


Figure 9: (a) Displacements of control point A at the end of the elastic beam and (b) lift and drag forces for parameter set II (Table 1).

Table 2: Values of oscillating quantities obtained by a fit of the form $[A \cdot \sin(2\pi \cdot f \cdot t + \phi) + M]$

Sets	I (FSI3)			II		
	M [m]	A [m]	f [Hz]	M [m]	A [m]	f [Hz]
$u_{s,x}$	$-2.55e-3$	$2.31e-3$	10.45	$-6.21e-3$	$7.07e-3$	12.54
$u_{s,y}$	$1.37e-3$	$3.38e-2$	5.23	$1.83e-3$	$5.13e-2$	6.27
	M [N]	A [N]	f [Hz]	M [N]	A [N]	f [Hz]
drag	421.10	31.28	10.44	489.02	67.63	12.54
lift	3.95	140.68	5.23	1.755	56.17	6.24

4.1.1. Convergence Studies

The Turek–Hron FSI3 benchmark is solved on a series of refined meshes to study convergence in space. The fluid domain is discretized on an $M \times N$ cartesian grid, and the Lagrangian domain is discretized using a mesh of linear elements (\mathbb{P}_1) with a space discretization step equal to $h_{si} = \{1.5 \cdot 10^{-3}, 3.10 \cdot 10^{-3}, 5.2 \cdot 10^{-3}, 1.0 \cdot 10^{-2}\}[\text{m}]$. The sizes of the resulting fluid grids and solid meshes are reported in Table 3.

Table 3: Fluid Grid and Solid Mesh refinements.

	Fluid Grid Points	Solid Mesh Elements/Nodes
(i=1) coarse	576×96	479/ 310
(i=2) medium	769×128	1179/ 686
(i=3) fine	1153×193	3286/ 1805
(i=4) finest	2304×384	14753/ 7710
reference	4608×762	44259/23130

A relative L^2 -norm error $e^h(\theta^h) = \|\theta^h - \theta^r\|_2 / \|\theta^r\|_2$ of a generic variable θ^h is computed with respect to the reference solution θ^r obtained with the highest resolution (Table 3). As can be observed in Figure 10 the displacement field shows a convergence rate between first and second order, whereas fluid pressure and velocity fields converge nearly quadratically.

The convergence in time is analyzed by adopting the finest spatial grid for fluid and solid and a time discretization parameter Δt equal to $\{5 \cdot 10^{-5}, 2.5 \cdot 10^{-5}, 1.25 \cdot 10^{-5}, 0.625 \cdot 10^{-5}\}[\text{s}]$. An L^2 -norm error $e^\tau(\theta^\tau) = \|\theta^\tau - \theta^r\|_2$ is computed at $t = 4.8[\text{s}]$ for a generic variable θ^τ with respect to a reference solution θ^r , obtained by using a time step of $0.15 \cdot 10^{-5}[\text{s}]$. The results in Figure 11 show that second order convergence rate is obtained for the variables.

4.2. Flow-induced oscillation of an inert plate

In this section, we present a benchmark for the treatment of inertial forces. This benchmark has an exact analytical solution (details are given in the Ap-

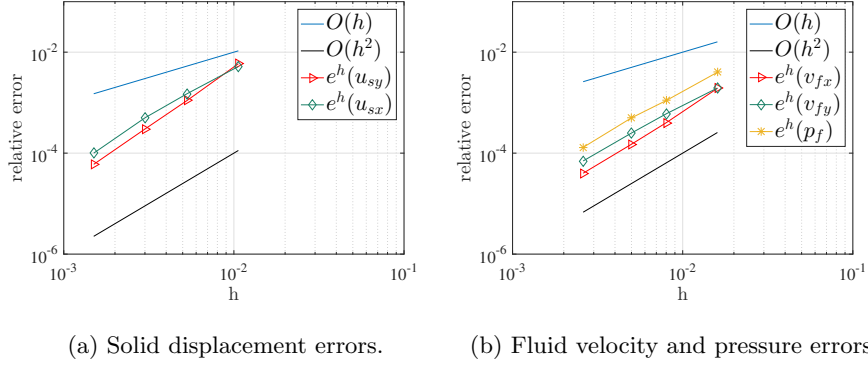


Figure 10: Relative errors $e^h(u_{sx})$, $e^h(u_{sy})$, $e^h(v_{fx})$, $e^h(v_{fy})$ and $e^h(p_f)$ in space of x - and y -components of solid displacements \mathbf{u}_s and fluid velocities \mathbf{v}_f and pressure p_f , respectively. Lines with slopes of $O(h)$ and $O(h^2)$ are shown for reference.

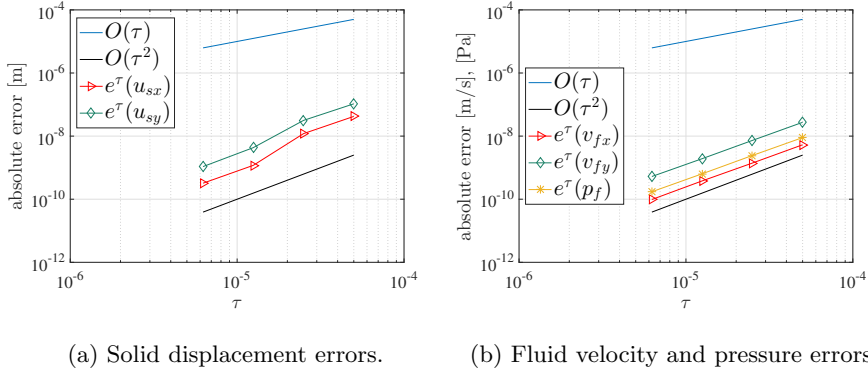


Figure 11: Absolute errors $e^\tau(u_{sx})$, $e^\tau(u_{sy})$, $e^\tau(v_{fx})$, $e^\tau(v_{fy})$ and $e^\tau(p_f)$ in time of x - and y -components of solid displacements \mathbf{u}_s and fluid velocities \mathbf{v}_f and pressure p_f in the L^2 -norm for $t = 4.8$ [s]. Lines with slopes of $O(\tau)$ and $O(\tau^2)$ are shown for reference.

pendix A). It consists of an infinitely long plate of thickness $2\delta_s$ immersed in a Newtonian incompressible fluid driven by an oscillating pressure gradient. The wall shear stresses on the surface of the plate induce an oscillation of the plate. For very light plates and slow frequencies the plate will oscillate synchronously with the fluid. For very heavy plates and high frequencies, the plate will experience only small oscillation amplitudes and a significant phase lag. It can be shown that the oscillation of the plate (amplitude and phase lag) is governed by a single parameter β (Equation (A.10)) which is built with the solid/fluid density ratio ρ_s/ρ_f and the Womersley number $\delta_s\sqrt{(2\pi f_0/\nu_f)}$, where $\nu_f = \mu_f/\rho_f$ is the kinematic viscosity.

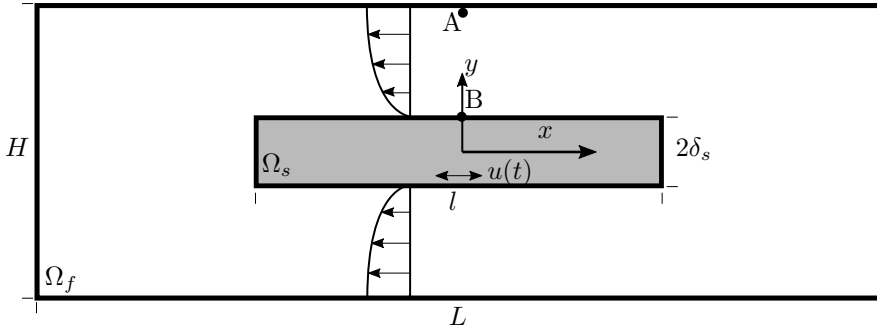


Figure 12: Geometry for the flow-induced oscillation benchmark. Data is sampled at extraction points A (fluid) and B (solid).

In the numerical experiments presented herein, the infinitely long plate is modelled as a two-dimensional beam with finite length $l \gg \delta_s$ located in the middle of the fluid channel as shown in Figure 12. We set $l = 1$ [m] and $\delta_s = 0.006$ [m], whereas the dimensions of the fluid domain are: length $L = 2$ [m], height $H = 0.2$ [m]. The center of the plate and of the fluid domain is located at $y = 0$. Periodic boundary conditions are imposed on all boundaries of the fluid domain, whereas a forcing term $\partial p/\partial x = G \cos(2\pi f_0 t)$ is applied over the entire domain with frequency $f_0 = 10$ [Hz] and $G = 110500$ [Pa]/ 2.2 [m] = 50227 [Pa/m]. To this aim, the nondimensional forcing term in the fringe region is modified as

follows:

$$\tilde{\mathbf{f}}_{\text{fringe}} = \left[G \cdot \frac{L_{\text{ref}}}{\rho_f U_{\text{ref}}^2} \right] \cos(2\pi f_0 L_{\text{ref}} / U_{\text{ref}} \tilde{t}). \quad (38)$$

In order to study the motion of the inert plate as a function of the parameter β , we consider physical parameters for three different test cases as indicated in Table 4 and model the solid material as linear elastic with $E = 20.0$ [MPa] and $\nu = 0.4$. Only reaction forces on the top and bottom edges of the plate are communicated in order to exclude normal forces on the edges that are normal to the flow. These edges are not present in the analytic formulation of the problem where an infinitely long domain is assumed.

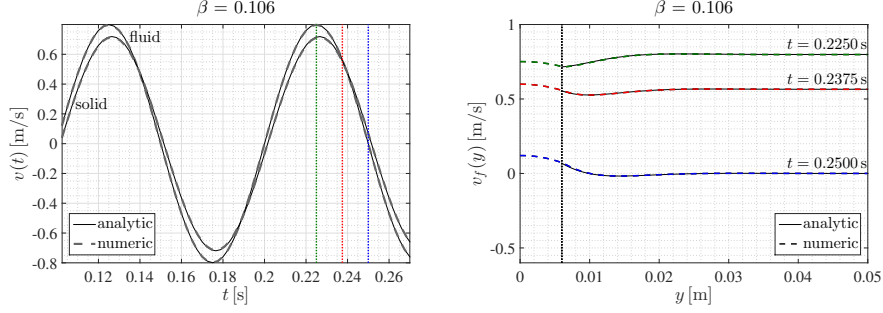
Table 4: Parameter settings for the flow-induced oscillations of a inert plate benchmark.

test case	ρ_s [kg/m ³]	ρ_f [kg/m ³]	μ_f [kg s ² /m]	β
A	100	1000	1.0	0.106
B	1000	1000	1.0	1.06
C	1000	1000	0.01	10.6

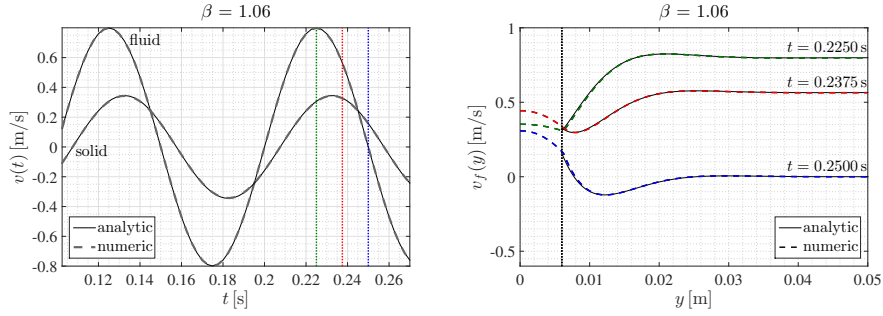
We use \mathbb{P}_1 finite elements for the space discretization of the solid subproblem and, as for the Turek–Hron benchmark, attach bilinear basis functions (\mathbb{Q}_1) to the fluid grid. The fluid domain is discretized using a 2048×129 Cartesian grid whereas the solid domain is discretized with a triangular mesh with a space discretization step equal to $h_s = 0.001$.

Figure 13 (left) shows the fluid velocity v_f at point A and solid velocities at point B for all three test cases ($\beta = 0.106, 1.06, 10.6$). The numerical results show a good agreement with the analytical solution (solid lines) for fluid and structure.

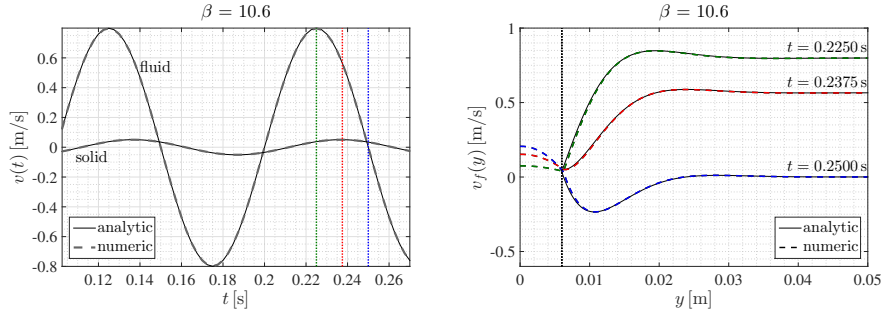
On the right, Figure 13 shows the velocity profiles $v_f(y)$ obtained along a vertical section in the middle of the flow channel at times $t = 0.225, 0.2375, 0.25$ [s]. Given the symmetry of the problem, we only show profiles for $y > 0$. The black dotted line represents the location of the fluid-structure interface at $y = \delta_s$. One may observe that (I) a Stokes boundary layer is established near the inert plate, and that (II) each numerical velocity profile (dashed line) recovers the related



(a) Test case A



(b) Test case B



(c) Test case C

Figure 13: Velocity profiles over time and space of the test cases summarized in Table 4. Left: Fluid and solid velocities over time at probe points A and B (Figure 12), respectively. Right: Fluid velocity profiles in the middle of the flow channel. Solid lines refer to the analytical solution and dashed lines refer to the numerical values. The time instances at which the velocity profiles were extracted are highlighted in their respective color in the plots on the left. Numerical results for the fluid velocity are also plotted within the solid domain $y < \delta_s$.

analytical one (solid line) very well for all the three tests cases.

Table 5: Comparison between the numerical and analytical values of the magnitude of the amplitude ratio $|\mathcal{A}|$ and of its phase-lag $\phi(\mathcal{A})$ for the three test cases (Table 4).

β	$\phi(\mathcal{A})$ [$^\circ$]	$\phi(\mathcal{A}_{an})$ [$^\circ$]	$\frac{ \phi(\mathcal{A}_{an}) - \phi(\mathcal{A}) }{ \phi(\mathcal{A}_{an}) }$	$ \mathcal{A} $	$ \mathcal{A} _{an}$	$\frac{ \mathcal{A} _{an} - \mathcal{A} }{ \mathcal{A} _{an}}$
0.106	-5.45	-5.47	0.36%	0.898	0.90	0.22%
1.06	-27.13	-27.22	0.33%	0.4305	0.4316	0.25%
10.6	-42.21	-42.42	0.49%	0.0633	0.0636	0.47%

Table 5 shows a quantitative comparison between the numerical results and the analytical solution (Equation A.16) for the magnitude of the amplitude ratio ($|\mathcal{A}|$) and the phase-lag ($\phi(\mathcal{A})$). The results indicate a relative error less than 0.5%.

4.3. Towards cardiovascular applications: Elastic beam in a 3D fluid channel

It is well known that human soft tissue is highly deformable and characterized by nonlinear and anisotropic behavior which requires the use of suitable anisotropic hyperelastic fiber-reinforced constitutive models. To this aim, we illustrate the capabilities of our FSI framework with a three-dimensional application consisting of an elastic beam immersed in a channel flow. We employ the constitutive law proposed by Holzapfel (Equation (3)) for modelling the anisotropic elastic behavior of human arterial walls and choose parameters for the fluid, which yield a Reynolds number regime typical of large blood vessels.

Let Ω_f be a three-dimensional fluid channel with extents $L_{f,x} = 0.07$ [m], $L_{f,y} = 0.03$ [m] and $L_{f,z} = 0.027$ [m], and Ω_s be a parallelepiped with dimensions: $L_{s,x} = 0.00115$ [m], $L_{s,y} = 0.02$ [m] and $L_{s,z} = 0.012$ [m] attached to the bottom wall of the fluid channel at $x = 0.02$ [m].

The fluid domain is discretized with a stretched Cartesian grid consisting of $161 \times 97 \times 97 = 1514849$ points, whereas the solid beam consists of 19838 \mathbb{P}_1 elements and 4555 nodes (Figure 14). \mathbb{Q}_1 basis functions are attached to the finite difference fluid grid for computing the transfer operator.

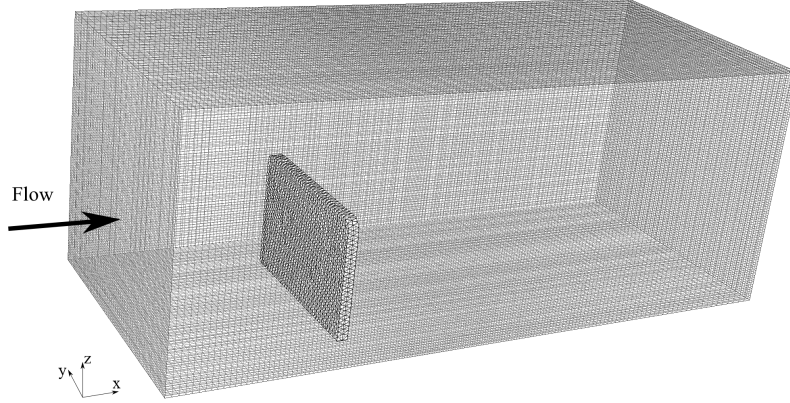


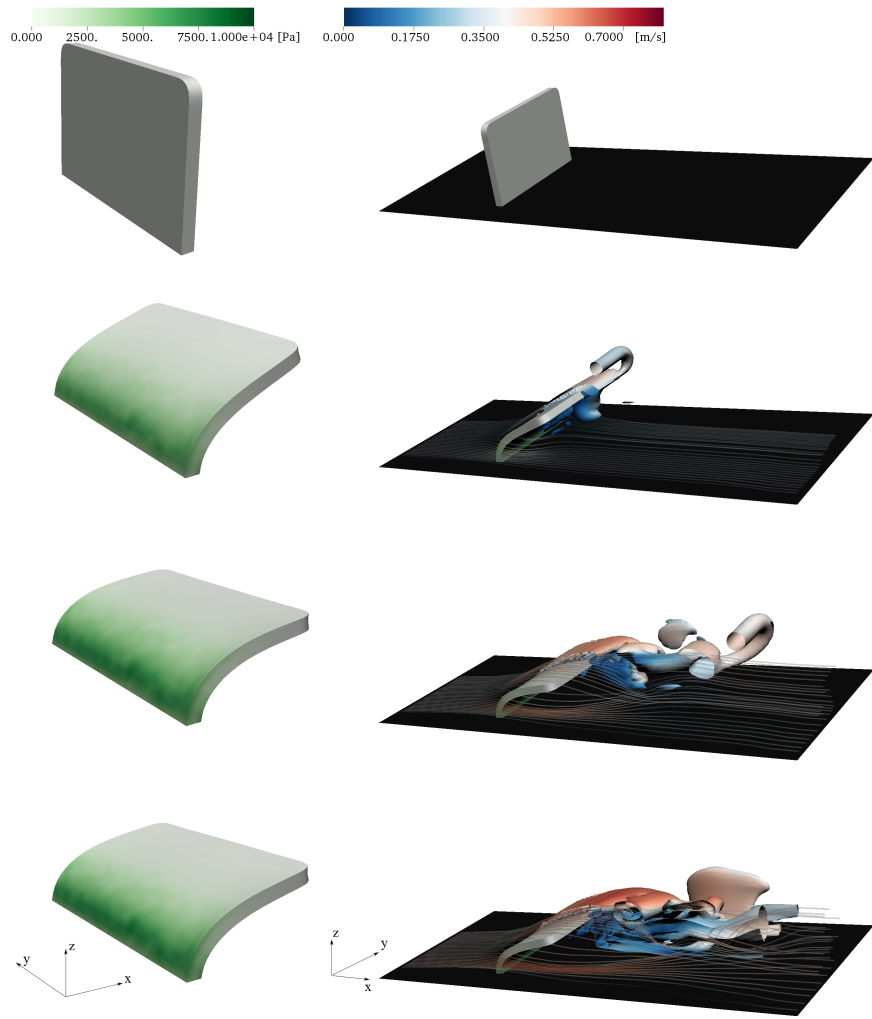
Figure 14: Mesh Setup for the 3D benchmark. The fluid grid consists of $161 \times 97 \times 97 = 1514849$ points, the solid mesh consists of 4555 nodes and 19838 tetrahedral elements.

We set the fluid density to $\rho_f = 1000$ [kg/m³], the reference length to $L_{\text{ref}} = L_{f,z} = 0.027$ [m] and the dynamic viscosity $\mu_f = 0.006$ [Pa · s], which leads to a Reynolds number of 2250. The solid structure and the fluid have the same density, and a nearly incompressible Holzapfel–Ogden material model is used with $\mu_s = 10$ [kPa], $\kappa = 1$ [MPa], $k_{11} = 10$ [kPa] and $k_{12} = 10$ [kPa]. A local base $\mathbf{e}_1, \mathbf{e}_2, \mathbf{e}_3$ is assumed with \mathbf{e}_1 oriented along the z -direction (i.e. $\mathbf{g}_{01} = 0\mathbf{e}_1 + 0\mathbf{e}_2 + 1\mathbf{e}_3$).

Periodic boundary conditions are imposed along the inlet and the outlet of the fluid channel together with no-slip boundary conditions on the lateral surfaces of the fluid channel. The flow is driven uniformly by a forcing region with parameters: $x_{\text{start}} = 0.0935$ [m], $x_{\text{end}} = 0.1$ [m] and $\hat{\lambda} = 10$.

The mechanical response of the elastic beam is characterized by computing the von Mises stress (\mathcal{VM}) [41] which represent a scalar field quantity widely used to predict yielding failure of ductile materials subjected to any loading condition. The spatial distributions of \mathcal{VM} at times $t = 0, 0.055, 0.11, 0.18$ [s] depicted in Figure 15a show uniformly distributed stresses.

Finally, Figure 15b depicts the same beam together with streamlines and isosurfaces for vortical structures (λ_2 -criterion, [40]). Both streamlines and



(a) von Mises Stresses

(b) Streamlines and λ_2 isosurfaces

Figure 15: Snapshots of the three-dimensional flexible membrane at times $t = 0, 0.055, 0.11, 0.18$ [s] immersed in a channel flow at $\text{Re}=2250$. (a) spatial distribution of the von Mises stresses of the solid structure. (b) streamlines and isosurfaces for $\lambda_2 = -0.54$ [40] colored by the local velocity magnitude.

isosurfaces are colored by the local velocity magnitude of the flow. The flow evolves from rest to a transitional character with an initial starting vortex shed from the top of the beam (see supplementary video). The starting vortex is advected out of the domain at which point more complex vortical structures start shedding from the top and the sides of the beam.

5. Conclusion

In this paper we have proposed a novel FSI framework based on the IBM. The main contribution consists of three key advancements with respect to existing immersed methodologies.

First, the use of L^2 -projections for the transfer of discrete data fields between nonconforming overlapping meshes ensures a modular and flexible coupling of independent flow and structure solvers based on different schemes for the time and space discretization. The current implementation of the variational transfer is based on piecewise affine meshes which allow for an efficient generation of the quadrature points for integrating in the intersection region. The proposed methodology can be extended to nonaffine meshes if high-order elements are adopted for the discretization of the solid subproblem.

Second, the description of the solid motion by the elastodynamics equations is solved via a fully implicit time integration scheme, which yields a robust scheme for structural dynamics.

Third, the use of high-order finite difference methods for the flow solver allows for the DNS of laminar, transitional and turbulent flows interacting with complex structures.

The benchmark results validate the framework with respect to the elastodynamics formulation, the flow solver, the fluid-structure interaction and the treatment of solid inertia. Furthermore, they demonstrate its capability of combining complex materials with flows at moderately high Reynolds numbers. The method is shown to be second-order accurate by means of a mesh- and time step-refinement study.

The present framework is thus able to solve the FSI of hyperelastic, non-homogeneous and anisotropic structures, immersed in incompressible laminar, transitional or turbulent flow. This makes it a promising tool for biomedical applications such as cardiovascular flow systems.

6. Acknowledgments

This research was supported by the Platform for Advanced Scientific Computing (PASC, <http://www.pasc-ch.org>) under the AV-FLOW project (<http://www.pasc-ch.org/projects/2013-2016/av-flow>). The authors also acknowledge the support of the Swiss National Supercomputing Centre (CSCS, [cscs.ch](http://www.cscs.ch)).

Declarations of interest: none

Appendix A. Analytical Inertia Benchmark

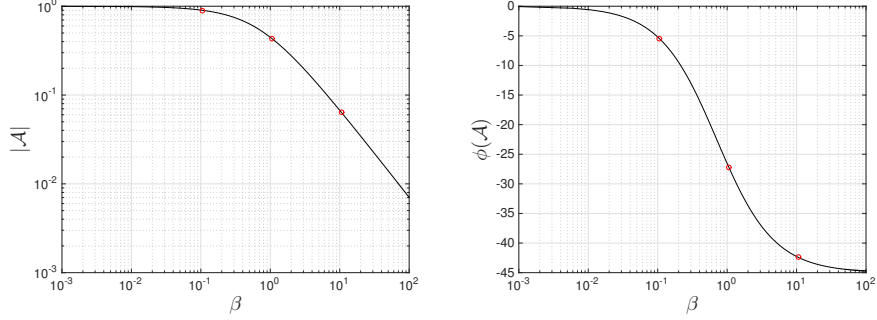


Figure A.16: Magnitude and phase diagram of the *amplitude* function $\mathcal{A}(\beta)$. The red spots indicate the test cases analyzed in Section 4.2.

We start considering the case of a viscous fluid near a wall, driven by an oscillating pressure gradient. With assumption of laminar flow and thus nearly parallel streamlines we can drop the advective term in the Navier–Stokes equations. Moreover, since the plate is supposed to be infinitely wide and long, the flow is invariant along the x -direction, i.e. $\frac{\partial(\cdot)}{\partial x}$ and from the continuity we see that $\frac{\partial u}{\partial x} = 0$. The unsteady Navier–Stokes equations reduce to:

$$\rho_f \frac{\partial v_f}{\partial t} = -\frac{\partial p}{\partial x} + \mu_f \frac{\partial^2 v_f}{\partial x^2}. \quad (\text{A.1})$$

The motion of the solid plate is forced by the viscous forces as follows:

$$2\delta_s \rho_s \frac{\partial v_s}{\partial t} = 2\tau. \quad (\text{A.2})$$

Here $2\delta_s$ is the thickness of the plate, and τ is the shear stress applied from the fluid to the solid. Moreover, the following conditions have to be fulfilled on the fluid-structure interface:

$$\tau = \mu \frac{\partial v_f}{\partial y}, \quad (\text{A.3})$$

$$v_s = v_f. \quad (\text{A.4})$$

By assuming the flow driven from a periodic pressure gradient, i.e. $\frac{\partial p}{\partial x} = -Ge^{j2\pi f_0 t}$, we will have to choose an ansatz for $u(y, t)$ that is periodic as well

and given the steady-state flow we can assume the frequency of the pressure profile as main frequency of the solution. Thus our ansatz becomes

$$v_f(y, t) = \mathcal{R}e\{V_f(y)e^{j2\pi f_0 t}\}, \quad (\text{A.5})$$

$$v_s(t) = \mathcal{R}e\{V_s e^{j2\pi f_0 t}\}. \quad (\text{A.6})$$

Plugging this into Equation (A.1), assuming that the velocity is bounded for $y \rightarrow \infty$ and using the boundary conditions on the interface (A.3) we get the following solution:

$$V_f(y) = \mathcal{R}e \left\{ v_{f,\infty} \left(1 - \frac{2\beta j}{1+j+2\beta j} e^{(1+j)\alpha} e^{-(1+j)\alpha \frac{y}{h}} \right) \right\}, \quad (\text{A.7})$$

where j is the imaginary unit, $v_{f,\infty}$ is the *free stream* velocity with

$$v_{f,\infty} := -\frac{jG}{2\pi f_0 \rho_f}, \quad (\text{A.8})$$

$$\alpha := \delta_s \sqrt{\frac{2\pi f_0 \rho_f}{2\mu}}, \quad (\text{A.9})$$

$$\beta := \frac{\rho_s}{\rho_f} \alpha \quad (\text{A.10})$$

and G is the amplitude of the pressure gradient, f_0 is the frequency of the oscillating driving pressure gradient and $h = 2\delta_s$ is the thickness of the solid plate.

The evaluation of the fluid velocity at $y = \delta_s$ gives the velocity of the solid plate which reads

$$V_s = V_f(y = \delta_s) = \mathcal{R}e \left\{ v_{f,\infty} \left(1 - \frac{2\beta j}{1+j+2\beta j} \right) \right\}. \quad (\text{A.11})$$

From here the *amplitude* ratio $\mathcal{A} := v_s/v_{f,\infty}$ is derived, which gives (i) the amplitude of the velocity oscillation v_s of the inert plate with respect to the amplitude of the oscillations of the *free stream* velocity $v_{f,\infty}$ and (ii) the phase lag between the two, both depending on β as follows :

$$\mathcal{A}(\beta) = 1 - \frac{2\beta}{2\beta + 1 - j}. \quad (\text{A.12})$$

The magnitude $|\mathcal{A}|$ and the phase spectrum $\phi(\mathcal{A})$ of the *amplitude* ratio $\mathcal{A}(\beta)$ are shown in Figure A.16.

References

References

- [1] C. S. Peskin, Flow patterns around heart valves: a numerical method, *Journal of computational physics* 10 (2) (1972) 252–271.
- [2] C. S. Peskin, The immersed boundary method, *Acta numer.* 11 (2002) 479–517.
- [3] W. K. Liu, Y. Liu, D. Farrell, L. Zhang, X. S. Wang, Y. Fukui, N. Patankar, Y. Zhang, C. Bajaj, J. Lee, J. Hong, X. Chen, H. Hsu, Immersed finite element method and its applications to biological systems, *Comput. Method Appl. M.* 195 (13) (2006) 1722–1749.
- [4] D. Kamensky, M. Hsu, D. Schillinger, J. Evans, A. Aggarwal, Y. Bazilevs, M. Sacks, T. Hughes, A variational immersed boundary framework for fluid-structure interaction: Isogeometric implementation and application to bioprosthetic heart valves, *Computer Methods in Applied Mechanics and Engineering* (2014) 2.
- [5] M. D. de Tullio, G. Pascazio, A moving-least-squares immersed boundary method for simulating the fluid–structure interaction of elastic bodies with arbitrary thickness, *Journal of Computational Physics* 325 (2016) 201–225.
- [6] B. E. Griffith, X. Luo, D. M. McQueen, C. S. Peskin, Simulating the fluid dynamics of natural and prosthetic heart valves using the immersed boundary method, *International Journal of Applied Mechanics* 1 (01) (2009) 137–177.
- [7] O. M. Mcgee, P. S. Gunning, L. M. Mcnamara, Computational characterization of bioprosthetic heart valve positioning to enhance long term performance, *Cardiology* 134 (2) (2016) 179.
- [8] M. De Tullio, A. Cristallo, E. Balaras, R. Verzicco, Direct numerical simulation of the pulsatile flow through an aortic bileaflet mechanical heart valve, *Journal of Fluid Mechanics* 622 (2009) 259–290.

- [9] M. Nobili, U. Morbiducci, R. Ponzini, C. Del Gaudio, A. Balducci, M. Grigioni, F. M. Montevecchi, A. Redaelli, Numerical simulation of the dynamics of a bileaflet prosthetic heart valve using a fluid–structure interaction approach, *Journal of biomechanics* 41 (11) (2008) 2539–2550.
- [10] J. Donea, A. Huerta, *Finite element methods for flow problems*, John Wiley & Sons, 2003.
- [11] J. Donea, A. Huerta, J. Ponthot, A. Rodriguez-Ferran, Arbitrary lagrangian eulerian methods, chapter 14, vol. 1: Fundamentals in encyclopedia of computational mechanics, Wiley, New York.
- [12] R. Mittal, G. Iaccarino, Immersed boundary methods, *Ann. Rev. Fluid Mech.* 37 (2005) 239–261.
- [13] L. Zhang, M. Gay, Immersed finite element method for fluid-structure interactions, *J. Fluid Struct.* 23 (6) (2007) 839–857.
- [14] M. G. Nestola, A. Gizzi, C. Cherubini, S. Filippi, Three-band decomposition analysis in multiscale fsi models of abdominal aortic aneurysms, *Int. J. Mod. Phys. C* 27 (02) (2016) 1650017.
- [15] D. Devendran, C. S. Peskin, An immersed boundary energy-based method for incompressible viscoelasticity, *J. Comput. Phys.* 231 (14) (2012) 4613–4642.
- [16] B. E. Griffith, X. Luo, Hybrid finite difference/finite element immersed boundary method, *International Journal for Numerical Methods in Biomedical Engineering* 33 (12) (2017) e2888–n/a, e2888 cnm.2888.
- [17] R. Mittal, H. Dong, M. Bozkurtas, F. Najjar, A. Vargas, A. von Loebbecke, A versatile sharp interface immersed boundary method for incompressible flows with complex boundaries, *J. Comput. Phys.* 227 (10) (2008) 4825–4852.

- [18] F. Sotiropoulos, I. Borazjani, A review of state-of-the-art numerical methods for simulating flow through mechanical heart valves, *Med. Biol. Eng. Comput.* 47 (3) (2009) 245–256.
- [19] D. Boffi, L. Gastaldi, A finite element approach for the immersed boundary method, *Comput. Struct.* 81 (8) (2003) 491–501.
- [20] R. Glowinski, Y. Kuznetsov, Distributed lagrange multipliers based on fictitious domain method for second order elliptic problems, *Comput. Method Appl. M.* 196 (8) (2007) 1498–1506.
- [21] F. P. Baaijens, A fictitious domain/mortar element method for fluid-structure interaction, *Int. J. Numer. Meth. Fl.* 35 (7) (2001) 743–761.
- [22] C. Hesch, A. Gil, A. A. Carreño, J. Bonet, P. Betsch, A mortar approach for fluid–structure interaction problems: Immersed strategies for deformable and rigid bodies, *Comput. Method Appl. M.* 278 (2014) 853–882.
- [23] J. Nitsche, Über ein variationsprinzip zur lösung von dirichlet-problemen bei verwendung von teilräumen, die keinen randbedingungen unterworfen sind, in: *Abhandlungen aus dem mathematischen Seminar der Universität Hamburg*, Vol. 36, Springer, 1971, pp. 9–15.
- [24] R. Krause, P. Zulian, A parallel approach to the variational transfer of discrete fields between arbitrarily distributed unstructured finite element meshes, *SIAM J. Sci. Comput.* 38 (3) (2016) C307–C333.
- [25] J. M. Melenk, I. Babuška, The partition of unity finite element method: basic theory and applications, *Computer methods in applied mechanics and engineering* 139 (1-4) (1996) 289–314.
- [26] G. A. Holzapfel, T. C. Gasser, R. W. Ogden, A new constitutive framework for arterial wall mechanics and a comparative study of material models, *Journal of elasticity and the physical science of solids* 61 (1-3) (2000) 1–48.

- [27] J. Chung, G. Hulbert, A time integration algorithm for structural dynamics with improved numerical dissipation: the generalized- α method, *J. Appl. Mech.* 60 (2) (1993) 371–375.
- [28] S. Erlicher, L. Bonaventura, O. S. Bursi, The analysis of the generalized- α method for non-linear dynamic problems, *Comput. Mech.* 28 (2) (2002) 83–104.
- [29] J. Williamson, Low-storage runge-kutta schemes, *J. Comput. Phys.* 35 (1) (1980) 48–56.
- [30] J. M. Stockie, B. R. Wetton, Analysis of stiffness in the immersed boundary method and implications for time-stepping schemes, *J. Comput. Phys.* 154 (1) (1999) 41–64.
- [31] R. Henniger, D. Obrist, L. Kleiser, High-order accurate solution of the incompressible navier–stokes equations on massively parallel computers, *J. Comput. Phys.* 229 (10) (2010) 3543–3572.
- [32] M. P. Simens, J. Jiménez, S. Hoyas, Y. Mizuno, A high-resolution code for turbulent boundary layers, *J. Comput. Phys.* 228 (11) (2009) 4218–4231.
- [33] P. Burns, E. Meiburg, Sediment-laden fresh water above salt water: non-linear simulations, *J. Fluid Mech.* 762 (2015) 156–195.
- [34] R. Henniger, L. Kleiser, E. Meiburg, Direct numerical simulations of particle transport in a model estuary, *J. Turbul.* (11) (2010) N39.
- [35] M. O. John, D. Obrist, L. Kleiser, Stabilisation of subcritical bypass transition in the leading-edge boundary layer by suction, *J. Turbul.* 15 (11) (2014) 795–805.
- [36] C. S. Peskin, B. F. Printz, Improved volume conservation in the computation of flows with immersed elastic boundaries, *Journal of computational physics* 105 (1) (1993) 33–46.

- [37] K. Fackeldey, D. Krause, R. Krause, C. Lenzen, Coupling molecular dynamics and continua with weak constraints, *Multiscale Model. Sim.* 9 (4) (2011) 1459–1494.
- [38] S. Turek, J. Hron, Proposal for numerical benchmarking of fluid-structure interaction between an elastic object and laminar incompressible flow, *Lecture notes in computational science and engineering* 53 (2006) 371.
- [39] J. Nordström, N. Nordin, D. Henningson, The fringe region technique and the fourier method used in the direct numerical simulation of spatially evolving viscous flows, *SIAM J. Sci. Comput.* 20 (4) (1999) 1365–1393.
- [40] J. Jeong, F. Hussain, On the identification of a vortex, *Journal of fluid mechanics* 285 (1995) 69–94.
- [41] F. A. Leckie, D. J. Bello, *Strength and stiffness of engineering systems*, Springer Science & Business Media, 2009.